LASER & PHOTONICS REVIEWS

www.lpr-journal.org

Spatial Control over Stable Light-Emission from AC-Driven CMOS-Compatible Quantum Mechanical Tunnel Junctions

*Fangwei Wang, Thanh Xuan Hoang, Hong-Son Chu, and Christian A. Nijhuis**

The potential application of quantum mechanical tunnel junctions as subdiffraction light or surface plasmon sources has been explored for decades, but it has been challenging to create devices with subwavelength spatial control over the light or plasmon excitation. This paper describes spatial control over the electrical excitation of surface-plasmon polaritons (SPPs) and photons in large-area junctions of the form of Al–AlO_X–Cu complementary metal-oxide-semiconductor (CMOS)-compatible tunnel junctions. Nanoscale spatial control (smallest feature sizes of 150 nm) is achieved by locally fine-tuning the thickness of the AlO_X tunneling barrier resulting in large local tunneling currents and associated SPP excitation rates. Mostly, plasmonic tunnel junctions are studied under DC operation with a relatively large bias (and associated currents) to observe light emission at optical frequencies. Large voltages risk device failure and reduce device lifetimes. Here it is demonstrated that the operational lifetime of AC-driven plasmonic tunnel junctions is improved by a factor of three. Under DC conditions, slow processes that lead to device failure (e.g., undesirable electromigration leading to shorts) readily occur, thus limiting the device decay time to 9.2 h; but under AC operation, such processes are slow with respect to the voltage changes prolonging the decay time beyond 18.0 h.

1. Introduction

Quantum mechanical tunnel junctions emit light due to inelastic electron tunneling where electrons cross a thin (1–3 nm) tunnel barrier sandwiched between two metal electrodes.[1] During inelastic tunneling, an electron loses a part of its energy to the excitations of photons and surface plasmon polaritons (SPPs). Subsequently, these SPPs can decay to photons via, for example, scattering induced by surface roughness in the electrodes or by incorporation of antennas.[2,3] Thus, these junctions can emit broadband light without the need for different emitters (such as quantum dots or molecules) in the vis–NIR spectral range depending on the electrode materials and the applied bias.[4–6] In so-called metal–insulator–metal (MIM) junctions, SPPs and photons can be readily excited, but these junctions usually have a large device area >>10 µm^2 and are based on Au or Ag electrodes that are not compatible with CMOS (complementary metal-oxide-semiconductor). In contrast, junctions based on scanning tunneling microscopy (STM) tips enable nanoscale spatial control over the excitation process; STM techniques, however, require dedicated tip configurations and bulky components, which are difficult to scale and apply in practical settings. In addition, tunnel junctions are typically studied under direct-current (DC) conditions which can cause electrical breakdown due to electromigration of metallic atoms and charge accumulation at the metal–oxide interface.[7–9] Mostly, electrical circuitry is operated under alternating current (AC) conditions where such issues are mitigated.

In this work, we report the stable operation of CMOS-compatible MIM junctions based on Al and Cu (materials that are widely used in back-end-of-line applications) under AC, rather than DC, conditions and demonstrate that it is possible to control light emission within the MIM junction area

F. Wang, C. A. Nijhuis
Department of Chemistry
National University of Singapore
3 Science Drive, Singapore 117543, Singapore
E-mail: c.a.nijhuis@utwente.nl

The ORCID identification number(s) for the author(s) of this article can be found under https://doi.org/10.1002/lpor.202100419

© 2022 The Authors. Laser & Photonics Reviews published by Wiley-VCH GmbH. This is an open access article under the terms of the Creative Commons Attribution-NonCommercial License, which permits use, distribution and reproduction in any medium, provided the original work is properly cited and is not used for commercial purposes.

DOI: 10.1002/lpor.202100419

T. X. Hoang, H.-S. Chu
Department of Electronics and Photonics
Institute of High Performance Computing
A*STAR (Agency for Science, Technology and Research), 1 Fusionopolis Way, #16-16 Connexis, Singapore 138632, Singapore

C. A. Nijhuis
Centre for Advanced 2D Materials and Graphene Research Centre
National University of Singapore
6 Science Drive 2, Singapore 117564, Singapore

C. A. Nijhuis
Hybrid Materials for Opto-Electronics Group, Department of Molecules and Materials, MESA+ Institute for Nanotechnology and Center for Brain-Inspired Nano Systems, Faculty of Science and Technology
University of Twente
P.O. Box 2017, Enschede 7500 AE, The Netherlands

18638899, 2022, 5, Downloaded from https://onlinelibrary.wiley.com/doi/10.1002/lpor.202100419 by University Of Twente Finance Department, Wiley Online Library on [18/01/2023]. See the Terms and Conditions (https://onlinelibrary.wiley.com/terms-and-conditions) on Wiley Online Library for rules of use; OA articles are governed by the applicable Creative Commons License

by local control over the tunneling barrier thickness. Since the first demonstration of light emission from a biased MIM junction[1], significant progress has been made to improve the electron-to-photon conversion efficiency up to 2% via the integration with optical antennas.[4,10–12] Inelastic tunneling can also be utilized to excite SPP modes propagating along plasmonic waveguides.[13–15] Directional control over SPPs and light emission has also been demonstrated via the integration of optical elements, such as gratings,[16] nanoantennas,[17] nanoparticles,[18] Yagi-Uda antennas,[19] and tilted self-assembled monolayers.[20] This paper describes a new method to manipulate the location of SPP/photon excitation within large-area junctions by tuning the tunneling current density via engineering of the tunnel oxide thickness. The tunneling current density J (A cm^{-2}) depends exponentially on the barrier thickness d (in nm) given by the general tunneling Equation[21]

$$J = J_0 \, e^{(-\beta d)} \tag{1}$$

where J_0 is a pre-exponential factor, and β (in nm^{-1}) is the tunneling decay coefficient. We use this exponential dependency of J on d to obtain spatial control over SPPs/photons excitation within large area MIM junctions. The SPP/photon excitation rate linearly scales with J, which, in turn, exponentially depends on d. By varying the local thickness of d, we can modulate the local SPPs/photons excitation rate in principle.

So far, most plasmonic tunnel junctions are made of Ag or Au that are not compatible with CMOS processes.[22–25] In contrast, Al and Cu are widely used in back-end-of-line applications in modern CMOS technologies. Recently, the renewed interest in copper was ignited with the demonstration of ultra low-loss copper hybrid plasmonic waveguides (propagation length > 40 μm)[26] and Cu nanowires sustaining high-quality plasmons (quality factors > 60).[27] Thus, copper is emerging as a cheap and high-quality plasmonic material, but oxidation of Cu is a concern. For these reasons, we report here plasmonic junctions of the form Al–AlO_X–Cu junctions coated with SiO_2 layer to prevent oxidation of the Cu surface.

Light emission from plasmonic tunnel junctions so far has been only studied under direct-current (DC) sources.[1–5,10–20] The unidirectional tunneling of electrons through the nanometer-thin layers results in undesirable electromigration of the metal atoms driven by the wind force or even the dielectric breakdown.[7] Such breakdown processes scale with the currents flowing across the junctions; nevertheless, relatively large currents are needed to observe light emission from the junctions with a large signal-to-noise ratio. In addition, the junctions are typically subjected to large voltages > 2 V (and associated current) to observe light emission in the visible range. To overcome this problem, we demonstrate that the operational lifetime of tunnel junctions driven by an alternating-current (AC) source, rather than a DC source, improves the stability of the devices by a factor of 3 despite large-applied voltages (and currents). The reason is that chemical processes are too slow to follow the changes in potential under AC conditions, significantly slowing down the processes that lead to catastrophic failure of the junctions.

2. Results and Discussion

2.1. The Device Schematic and the Working Principle

To demonstrate spatial control over SPPs/photons excitation within the junction area, we fabricated the lion logo of the National University of Singapore (NUS) by varying the oxide thickness. **Figure 1**a shows a schematic of the patterned Al–AlO_X–Cu tunnel junction. The AlO_X layer defines the tunnel barrier thickness, the Al electrode functions as the bottom electrode, and the Cu electrode forms the top electrode. We deposited a cladding of 100 nm thick SiO_2 on top of the Cu electrode to prevent Cu oxidation, so that the devices work well in the ambient environment. Figure 1b shows a cross-section illustration of the junction area. We thinned the oxide layer via a wet-etch; in these thin areas, the tunneling current will be much larger than in surrounding areas, as explained in the introduction (Equation 1); consequently, SPPs and photons are predominantly excited in these thin areas. Figure 1c shows the energy level diagram of a biased MIM junction. The light emission mechanism is attributed to inelastic electron tunneling (IET), where the electrons tunnel through the AlO_X barrier and lose energy to all available optical modes.[2,3] Figure S1 (Supporting Information) illustrates the fabrication flow of Al/$AlOx$/Cu tunnel junctions with the lion logo of NUS. Figure 1d shows the false-color scanning electron micrograph (SEM) image of the patterned Al–AlO_X–Cu tunnel junction array of 5 × 5 lion samples (the unmodified SEM image is shown in Figure S2 in the Supporting Information) before the SiO_2 cladding was deposited. The respective thickness of AlO_X beneath the patterned and un-patterned area was determined via impedance spectroscopy (**Table 1**). The smallest feature available is around 150 nm, well below the resolution limit of our optical microscope. Figure 1e shows a zoom-in SEM image on the single lion of 7 × 10 μm^2. Figure 1f illustrates the corresponding atomic force microscopy (AFM) image, showing that the thickness of the Al and Cu electrodes is 35 and 110 nm, respectively. We also estimated that the root mean square (RMS) surface roughness (induced by the wet-etch process) of the patterned junction area is around 4.2 ± 0.3 nm, which is more than threefold higher than that of the unpatterned area (1.2 ± 0.1 nm) (Figure S3, Supporting Information). We would also like to note that commonly used adhesion layers, e.g., Ti or Cr, to stabilize Au films are very lossy;[28,29] such adhesion layers were not necessary in the case of Cu.[30,31]

2.2. Electrical and Optical Characterization

We performed the electrical measurements by applying a voltage bias V to the Al electrode while the top Cu electrode was grounded. **Figure 2**a shows a typical nonlinear $I(V)$ curve along with a positive, parabolic differential conductance, dI/dV, which is characteristic of coherent tunneling (Figure 2b). We noted a small background capacitive current (<10 nA), which could have been caused by several reasons, such as the connections of the electrometer, cabling, or wiring.[32,33] For the sake of completion, we have plotted $\ln(I/V^2)$ against $1/V$ for Al–AlO_X–Cu planar tunnel junctions at room temperature. Figure S4 (Supporting Information) shows the transition voltages at the two polarities of

© 2022 The Authors. Laser & Photonics Reviews published by Wiley-VCH GmbH

18638899, 2022, 5, Downloaded from https://onlinelibrary.wiley.com/doi/10.1002/lpor.202100419 by University Of Twente Finance Department, Wiley Online Library on [18/01/2023]. See the Terms and Conditions (https://onlinelibrary.wiley.com/terms-and-conditions) on Wiley Online Library for rules of use; OA articles are governed by the applicable Creative Commons License

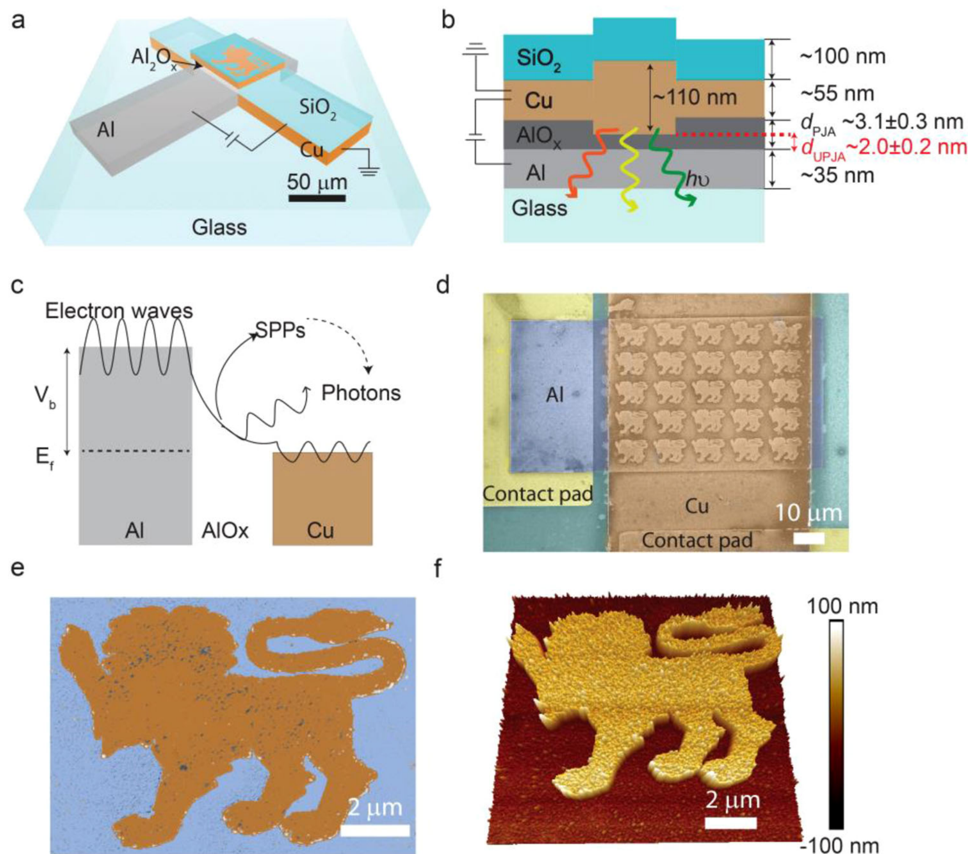

Figure 1. a) Schematic illustration of an Al–AlO_X–Cu tunnel junction patterned with the NUS lion logo. b) Cross-section profile of the junction, where d_{PJA} and d_{UPJA} denote the oxide thickness beneath the patterned junction area and unpatterned junction area, respectively. c) Energy level diagram of the junction showing the excitation mechanism of SPPs and photons. d) False-colour SEM image of an Al/AlO*x*/Cu tunnel junction with a 5 × 5 array of the NUS logo. e) zoom-in on a single lion along with its f) corresponding AFM image.

Table 1. Results of the Fits of the Equivalent Circuits to the Impedance Data.

Tunnel oxide[a)]	A_J	R_C[b)] [Ω]	R_J [MΩ][b)]	C_J [pF][b)]	d_{oxide} [nm]
Wet-Etched[c)]	5 × 5 μm^2	8300 ± 600	7.24 ± 0.07	0.96 ± 0.01	2.0 ± 0.2
Oxidized[d)]	20 × 20 μm^2	345 ± 24	1.75 ± 0.01	10.29 ± 0.03	3.1 ± 0.3

[a)] The experimental impedance data were fitted to the equivalent circuit (Figure 4a) using the complex nonlinear least-squares fitting method; [b)] The errors denote the standard deviation from the fitting result; [c)] The data were collected with a geometrical junction area of 5 × 5 μm^2; [d)] This tunnel junction has a large area of 20 × 20 μm^2 that ensures reliable measurements of the capacitance.

−1.17 and 0.79 V. We note that the transition voltages are much lower than expected for the tunneling barrier height defined by the AlO_X layer. However, it was well known that the transition voltages are also dependent on other factors such as the presence of defects (impurities), oxide barrier quality, and geometrical shape of electrodes (see additional discussion in Section S4 in the Supporting Information).[34–36] Thus, it is not straightforward to draw a meaningful conclusion regarding the charge transport mechanism from such Fowler–Nordheim plots .[13,37,38] We recorded the emitted light from the glass side of the junctions with an EMCCD camera and vis–NIR spectrometer using an integration time of 2 min. Figure 2c shows the EMCCD image of a 5 × 5 array of the NUS logo with an applied bias of $V = 1.5$ V. The light emission originated predominantly from the patterned junction area, where the corresponding oxide thickness (d_{PJA}) is relatively thin compared with the unpatterned junction area (d_{UPJA}); the thickness difference is estimated as $\Delta d = d_{UPJA} - d_{PJA} = 1.1$ nm (Table 1). Due to the exponential dependence of tunneling current on the oxide thickness (Equation 1), most electrons will tunnel through the patterned junction area resulting in predominant excitation of the SPPs/photons in those patterned areas. It is noteworthy that the wet-etching process roughened the patterned area furthermore (Figure S3, Supporting Information), enhancing the plasmon-to-photon conversion efficiency. Light emission from biased tunnel junctions mainly originated from scattered gap SPPs due to surface roughness in the electrodes. We have provided an analysis of the propagation of the gap SPPs in Figure S5 in the Supporting Information. The calculated propagation length of the gap SPP mode is around 43 nm, which is much shorter than the dimensions of the junction area. Hence, the observed light emission originates from immediate locations with substantial tunneling currents. The smallest feature size is 150 nm, as shown in the AFM image in Figure 1f, but our optical

© 2022 The Authors. Laser & Photonics Reviews published by Wiley-VCH GmbH

18638899, 2022, 5, Downloaded from https://onlinelibrary.wiley.com/doi/10.1002/lpor.202100419 by University Of Twente Finance Department, Wiley Online Library on [18/01/2023]. See the Terms and Conditions (https://onlinelibrary.wiley.com/terms-and-conditions) on Wiley Online Library for rules of use; OA articles are governed by the applicable Creative Commons License

18638899, 2022, 5, Downloaded from https://onlinelibrary.wiley.com/doi/10.1002/lpor.202100419 by University Of Twente Finance Department, Wiley Online Library on [18/01/2023]. See the Terms and Conditions (https://onlinelibrary.wiley.com/terms-and-conditions) on Wiley Online Library for rules of use; OA articles are governed by the applicable Creative Commons License

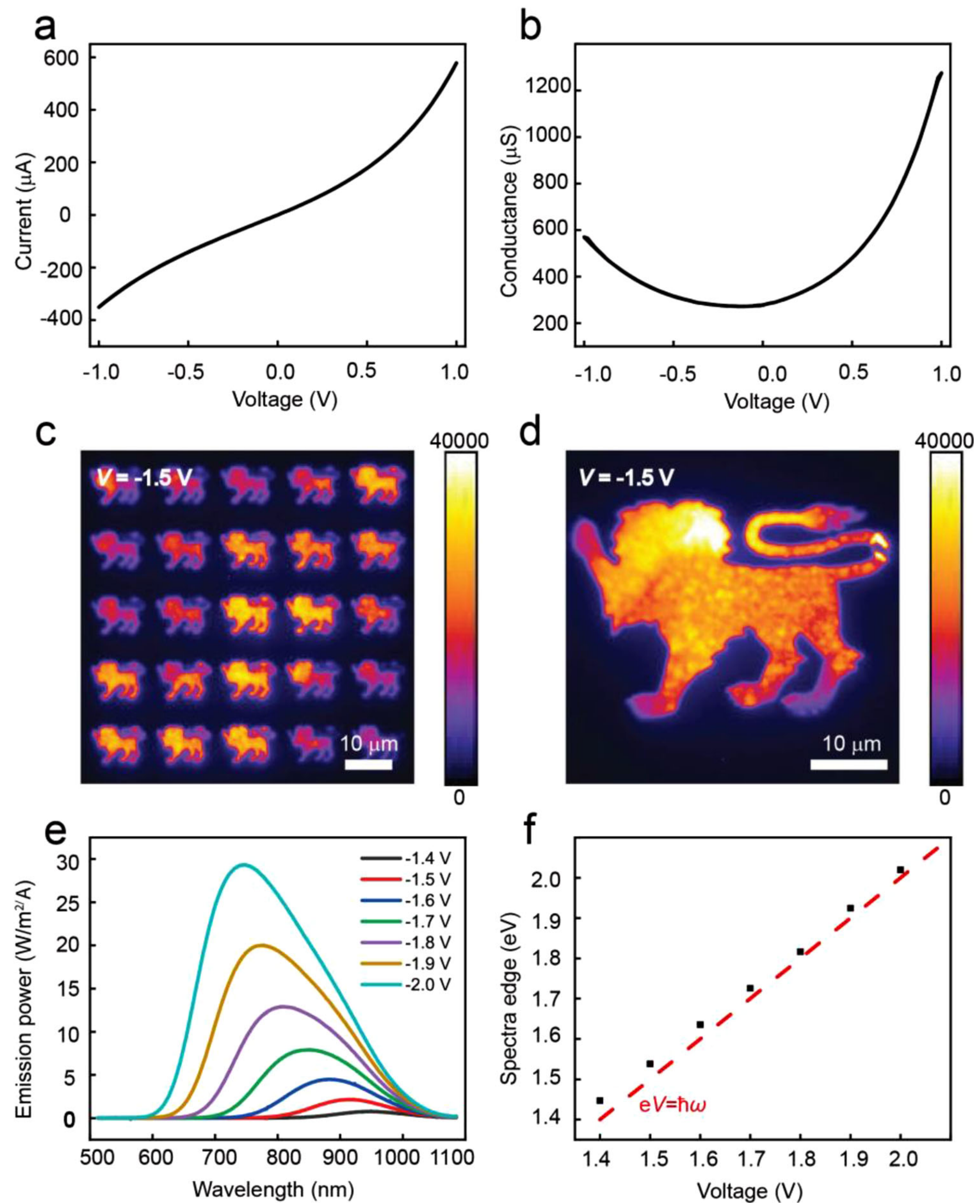

Figure 2. a) Current–voltage $I(V)$ curve of the patterned device showing the typical nonlinear electrical properties of tunnel junctions. b) Differential conductance dI/dV characterizations show parabolic behavior. c) EMCCD image of biased tunnel junction patterned with an array of 'NUS' logo (5 × 5) measured at V = -1.5 V. (**d**) EMCCD image of biased tunnel junction with one 'NUS' logo measured at $V = -1.5$ V. e) Spectral photon emission power collected at various voltages. f) Spectral edge as a function of V compared to the quantum cutoff (red dashed line).

measurements are diffraction-limited; therefore, this smallest feature sizes cannot be resolved. We also note that light emission efficiency depends on the dimensions of the tunnel junction, especially when the lateral junction dimensions approach the propagation length of gap SPP modes.[2,4,11] For demonstration purposes, we also fabricated a junction with one large lion of 45 × 65 μm, where the fine details of the lion are readily resolved (Figure 2d). To further demonstrate the potential application of the plasmonic display based on the patterned tunnel junction, Figure S6 (Supporting Information) demonstrates the collected light emission from another patterned tunnel junction comprising three letters "N," "U," and "S" via a similar procedure.

Figure 2e shows the typical broad vis–NIR spectra as a function of V, characteristic of plasmonic tunnel junctions. The spectra blueshift with increasing V, a clear signature for excitation by IET.[1,2] Light emission via IET follows the quantum cutoff law ($\hbar\omega \leq |eV|$), i.e., the energy of the emitted photons cannot exceed the energy of tunneling electrons. We plotted in Figure 2f the energy of tunneling electrons $\hbar\omega = |eV|$ and the maximum energy of the emitted photons (Figure S7, Supporting Information). The spectral edge depends linearly on the V, but there is a slight over bias light emission of $\hbar\omega_{max} - |eV| \approx 50$ meV signifying the contribution of hot electrons in the light emission process.[39,40] For completeness, we also fabricated and characterized the electrical

 © 2022 The Authors. Laser & Photonics Reviews published by Wiley-VCH GmbH

18638899, 2022, 5, Downloaded from https://onlinelibrary.wiley.com/doi/10.1002/lpor.202100419 by University Of Twente Finance Department, Wiley Online Library on [18/01/2023]. See the Terms and Conditions (https://onlinelibrary.wiley.com/terms-and-conditions) on Wiley Online Library for rules of use; OA articles are governed by the applicable Creative Commons License

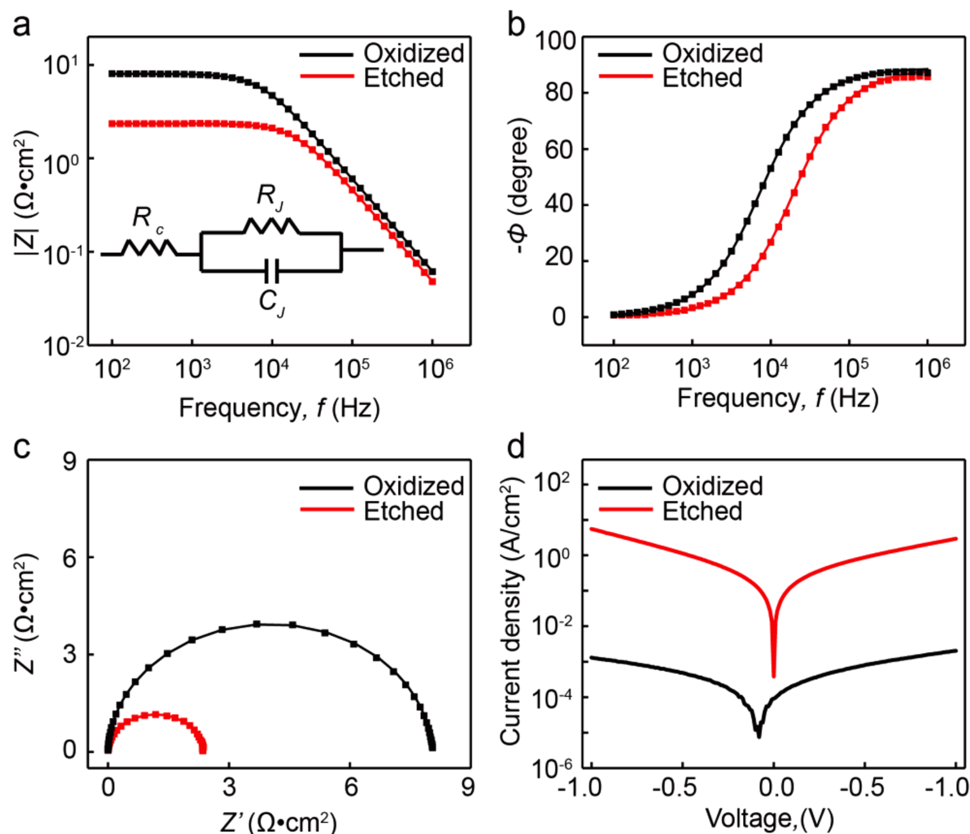

Figure 3. a) Frequency dependency of the impedance of two types of Al–AlO_X–Cu tunnel junctions (oxidized and etched). Inset shows the equivalent (symbols are explained in the text). b) Corresponding phase angle as a function of frequency and c) Nyquist plots. The solid lines are fit to the equivalent circuit shown in the inset in panel (a). d) $J(V)$ curves of the two Al–AlO_X–Cu TJs with the two different oxide thicknesses (etched and oxidized). The $J(V)$ curves were measured with a scan rate of 10 mV s^{-1}.

and optical performance of flat tunnel junctions without the pattern. Figure S8 (Supporting Information) demonstrates uniform light emission from the whole junction area, suggesting that tunnel oxide thickness is homogeneous across the junction area.

2.3. Tunneling Barrier Thickness Determination

To determine the corresponding oxide thickness of the patterned and unpatterned junction areas for the device shown in Figure 1, we fabricated another two planar Al–AlO_X–Cu tunnel junctions, following the same fabrication process (Figure S1, Supporting Information). For one junction, the Al bottom electrode is hot baked at 180 °C for 10 min for oxidized tunnel barrier AlO*x*, while the oxide of the other junction was wet etched and then regrown at ambient condition for 30 min. The oxide thicknesses of tunnel junctions were determined by impedance spectroscopy. The inset in **Figure 3**a shows the equivalent circuit of the tunnel junction where junction resistor (R_J) and capacitor (C_J) are connected in parallel, and both are connected in series with the contact resistor (R_C); this contact resistor represents the plasmonic waveguides. We carried out the impedance measurements in the frequency range from 100 Hz to 1.0 MHz using a sinusoidal signal with an amplitude of 30 mV at zero DC bias. Figure 3a shows the frequency dependency of the modulus of the complex impedance ($|Z|$) and a fit to the equivalent circuit from which we extracted R_J, R_C, and C_J (Table 1). We then determined the thickness of the tunnel junction using

$$C_J = \epsilon_0 \, \epsilon_{oxide} A_J / d_{oxide} \tag{2}$$

where ϵ_0 = vacuum permittivity; ϵ_{oxide} = relative permittivity of AlO_X ($\epsilon_{oxide} = 10$);[41] d_{oxide} = oxide thickness, and A_J = fabricated junction area. Figure 3b,c shows the phase spectra and Nyquist plot, respectively. These data show that the modulus of the complex impedance ($|Z|$) decreases significantly at high frequencies at which the phase shift $\phi \approx 90°$ since the capacitive reactance decreases with frequency; however, it remains almost constant at low frequencies ($\phi \approx 0°$), where the impedance is dominated by the resistance of the tunnel oxide. The Nyquist plot is dominated by a single semicircle. These observations indicate that these junctions can be represented by a single capacitor for both the etched and oxidized cases.

Table 1 shows our fitting results that $d_{oxide} = 3.1 \pm 0.3$ and 2.0 ± 0.2 nm for the oxidized and etched oxide, respectively. Hence, the difference of oxide thickness (Δd) in the patterned and unpattern junction area is roughly 1.1 nm. For this thickness difference, we can estimate the difference between the current density below the 'NUS' logo and that in the unpatterned area using Equation (1) with a tunneling decay coefficient of $\beta \approx 7.6$ nm^{-1}.[42–44]

© 2022 The Authors. Laser & Photonics Reviews published by Wiley-VCH GmbH

18638899, 2022, 5, Downloaded from https://onlinelibrary.wiley.com/doi/10.1002/lpor.202100419 by University Of Twente Finance Department, Wiley Online Library on [18/01/2023]. See the Terms and Conditions (https://onlinelibrary.wiley.com/terms-and-conditions) on Wiley Online Library for rules of use; OA articles are governed by the applicable Creative Commons License

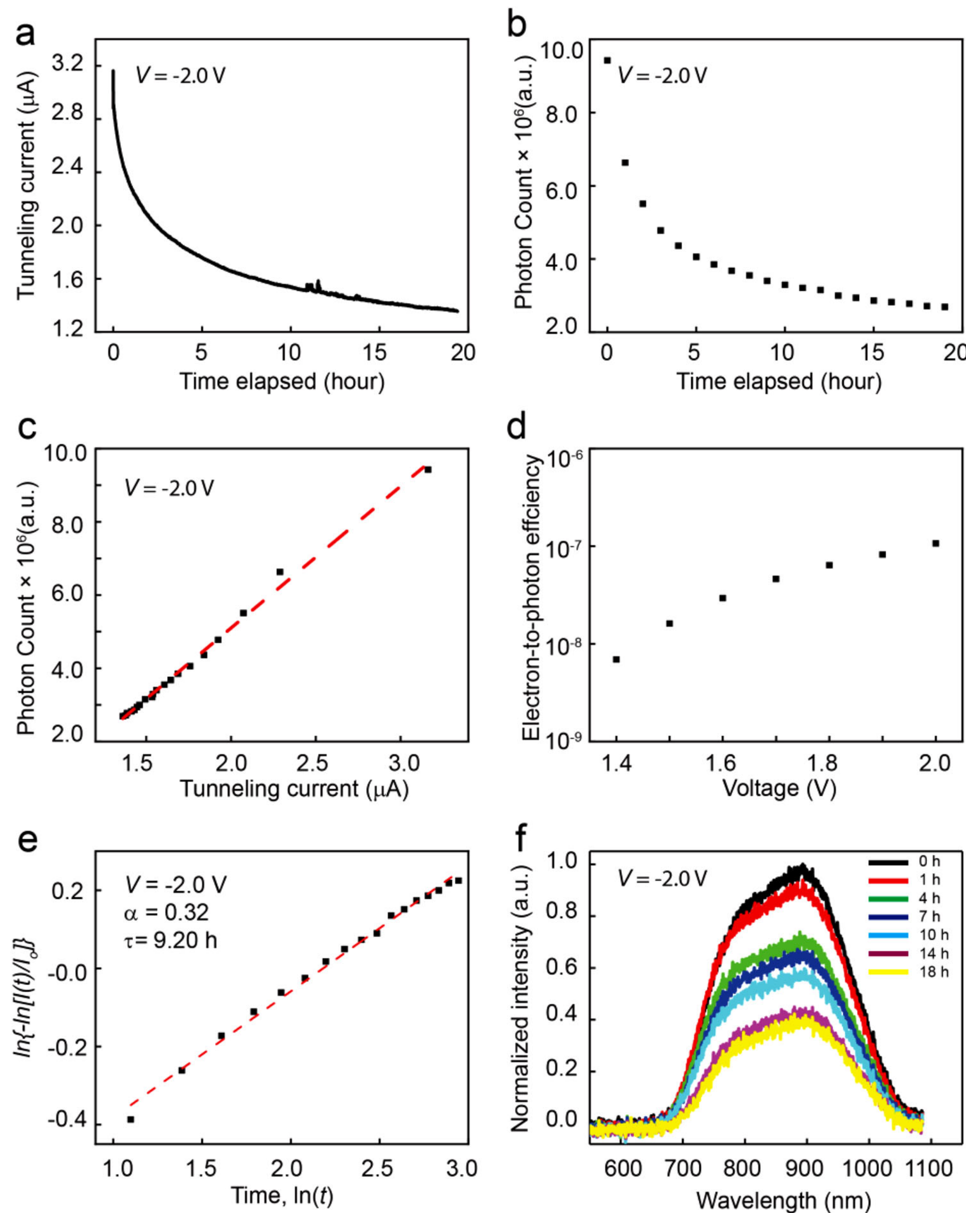

Figure 4. a) Recorded current as a function of operation time. The tunnel junction was biased at $V = -2.0$ V. b) Light emission intensity decays as a function of time elapsed. c) Collected light emission intensity plotted against the tunneling current. The dashed line is a visual guide. d) Emission Efficiency (photon per electron) as a function of V. e) Fit (dashed line) of the normalized light intensity as a function of time to Equation (3). f) Collected spectra from the tunnel junction at different operation intervals.

Theoretically, the current density tunneling through the 'NUS' logo is $e^{\beta \Delta d} \approx 4270$ times higher than in the unpatterned area. Experimentally, we measured the J(V) responses of the two tunnel junctions (oxidized and etched), as shown in Figure 3d. The experimental current density of the junction with the etched oxide is 10^3–10^4 higher than that of the other junction with oxidized tunneling barrier, which agrees well with the theoretical estimation via Equation (1). The exponential dependence of tunneling current density on the oxide thickness makes it possible to control the excitation location of SPPs/photons since most electrons will tunnel through the patterned junction area with relatively thinner oxide thickness.

2.4. DC-Driven Operational Lifetime

Figure 4 presents the light emission stability of the DC-driven unpatterned Al–AlO_X–Cu tunnel junctions. The device was biased at −2.0 V continuously for 18.0 h, and the time trace of tunneling current was recorded. Figure 4a shows that the tunneling current decreases as time lapses. Figure 4b illustrates the decay of the light emission intensity as a function of time. We found that the intensity decays to 50% after 6.0 h of operation and 25% after 18.0 h. Figure 4c shows the linear relationship between the light emission intensity and the tunneling current (in agreement with our prior work[13]), suggesting that the decay

© 2022 The Authors. Laser & Photonics Reviews published by Wiley-VCH GmbH

18638899, 2022, 5, Downloaded from https://onlinelibrary.wiley.com/doi/10.1002/lpor.202100419 by University Of Twente Finance Department, Wiley Online Library on [18/01/2023]. See the Terms and Conditions (https://onlinelibrary.wiley.com/terms-and-conditions) on Wiley Online Library for rules of use; OA articles are governed by the applicable Creative Commons License

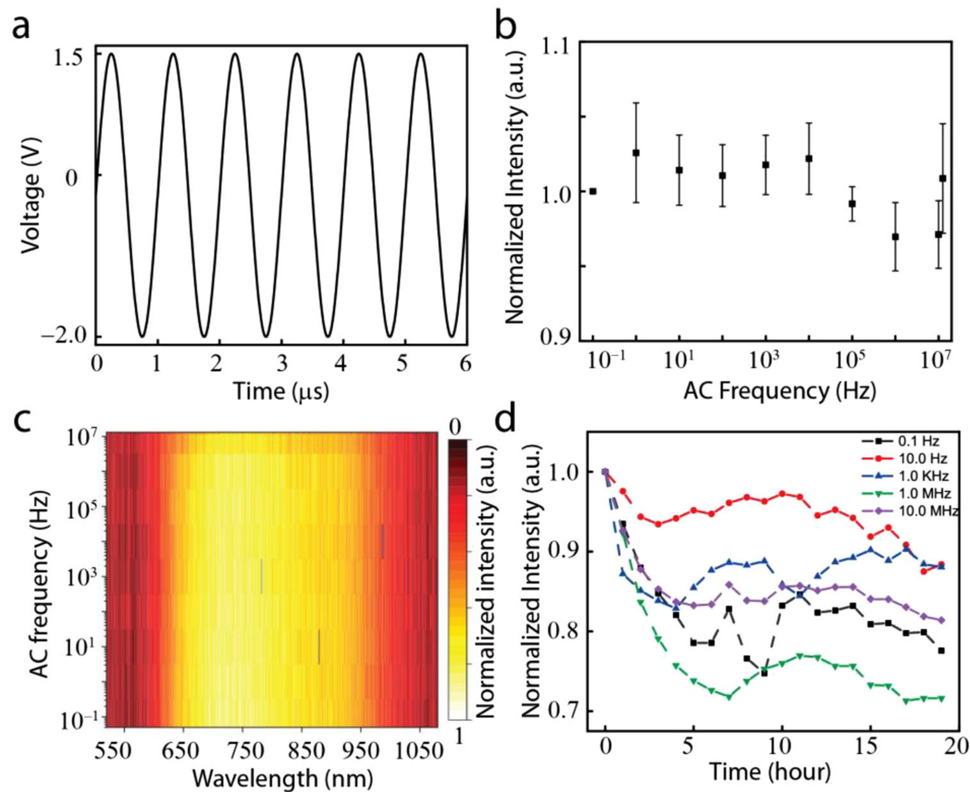

Figure 5. a) Time trace of the sinusoidal waveform of the applied voltage ranging from +1.5 to −2.0 V. b) Frequency-dependent light emission intensity averaged from three different tunnel junctions, which were biased with AC signals at different frequencies ranging from 0.1 Hz to 10.0 MHz. The light-emitting intensity was calculated via the collection of EMCCD images at each frequency. c) Heatmap of vis–NIR spectra collected at various AC frequencies from 0.1 Hz to 10.0 MHz. d) Time traces of the normalized light emission intensities were collected at different AC frequencies. The light emission intensity was normalized to values between 0 and 1.

of the light emission intensity is caused by a reduction of the tunneling current caused by junction degradation due to the applied DC bias and consequential unidirectional current flow. This degradation may be explained by metal oxide formation due to trapped water or oxygen (since the AlO_X layers were prepared ex situ in the ambient environment).

We have shown before that for other types of junctions the overall electron-plasmon outcoupling efficiency can be as high as 1.5% due to the presence of surface roughness provided the electrodes are very thin.[3,13,45] However, for most junctions, the electron-photon conversion efficiencies are on the order of 10^{-5}–10^{-7}.[11–13] Figure 4d illustrates that our junctions fall in this range with photon outcoupling efficiency of 4.0×10^7 counts/s (corrected by the detector's photon collection efficiency of 4%) and the number of electrons tunneling across the junctions (3.7×10^{14} electrons/s, $V = -2.0$ V). We fitted the curve in Figure 4b with the following stretched exponential Equation[46,47]

$$I(t)/I_0 = \exp[-(t/\tau)^\alpha] \tag{3}$$

where $I(t)$ and I_0 present the light emission intensity at a time (t) and initial intensity, respectively; τ is the decay time when intensity decays to $1/e$ of its initial value. For $\alpha = 1$ exponential decay function is ideal, while $0 < \alpha < 1$ suggests that the graph of log $I(t)$ versus t is characteristically stretched. The red dash line in Figure 4e presents the fit to Equation (3) to the measured light emission intensity as a function of t that results in $\alpha = 0.32$ and $\tau = 9.2$ h. For completeness, we also collected the light emission spectra at different operational times. Figure 4f shows that the spectral shape does not change as time elapses despite the time decay of the integrated intensity. This observation suggests that the changes in the tunneling barrier, though causing a rapid decay of the tunneling current, did not affect the optical properties of the junction. This result also explains the time-independent electron-photon conversion efficiency (Figure S9, Supporting Information).

2.5. AC-Driven Operational Lifetime

We investigated the light emission stability of AC-driven tunnel junctions using alternating sinusoidal waveform voltages with frequencies f ranging from 0.1 Hz to 10.0 MHz. **Figure 5**a illustrates the time trace of the applied alternating voltage (sinusoidal waveform) with an amplitude from 1.5 to −2.0 V with a period of 1.0 μs ($f = 1.0$ MHz). This asymmetrical voltage range accounts for the different breakdown voltages at forward and reverse bias (Figure S10, Supporting Information). Figure 5b shows the averaged light-emission intensity as a function of the applied AC frequency ranging from 0.1 Hz to 10.0 MHz (it is noted that light

© 2022 The Authors. Laser & Photonics Reviews published by Wiley-VCH GmbH

output changes instantaneously with the voltage at these such low frequencies[12]). Each point represents the initial intensity from an EMCCD image at a specific AC frequency with an integration time of 2 min. We normalized the light emission intensity with that of the 0.1 Hz for the convenience of comparison. The error bar represents the standard deviation measured over three different tunnel junctions. As is illustrated in Figure 5c, we have also collected the corresponding vis–NIR spectra of tunnel junctions at each driving frequency. We found that both initial light emission intensity and spectral shape remain constant when the AC frequency ranges from 0.1 Hz to 10.0 MHz, indicating that the optical environment of tunnel junctions is independent of the modulation frequency and the measurement time. Figure 5d shows the time traces of the light emission intensities collected at the respective AC frequency. Although AC operation gives a 3 times improvement in stability over DC operation, there is still a large device-to-device variation. The AC-driven light emission intensity remains greater than 70% of the initial value after working 18.0 h of continuous operation, while those DC-driven devices decay to 25% within 18.0 h. This lifetime improvement of tunnel junctions be readily explained as follows: electromigration and diffusion of atoms cannot follow the relatively fast periodical applied voltage and bidirectional current. We note that other types of commercial tunnel junctions fabricated under highly controlled conditions are stable for years;[48–50] hence, there is plenty of room for improvement in the fabrication of plasmonic tunnel junctions.

3. Conclusions

In summary, we present a new method to control the SPP/photon excitation location via engineering the tunnel oxide thickness. As a demonstration, EMCCD images patterned with 'NUS' logo arrays (5 × 5) and NUS' letters were collected at a low bias (−1.5 V) in CMOS-compatible tunnel junctions (since Al and Cu are commonly used in back-end-of-line applications). Light emission was observed predominantly from the patterned junction area as the corresponding oxide thickness of the patterned area is a nanometer (≈1.1 nm) thinner than the unpatterned area. Because of the sensitivity of the tunnel junctions to variations in the oxide thickness, our results are also potentially interesting in other areas of research as, in principle, information can be encoded in patterned tunnel junctions, which may find potential applications for anti-counterfeiting where it is important to create structures that cannot be duplicated,[51,52] or high-density optical storage.[53–55] We also demonstrated that the operational lifetime of the light source based on tunnel junctions could be significantly improved in AC mode. The concept resulting in this improvement is potentially useful for other studies involving plasmonic tunnel junctions.[56]

Supporting Information

Supporting Information is available from the Wiley Online Library or from the author.

Acknowledgements

The authors acknowledge the National Research Foundation (NRF) for supporting this research under the Prime Minister's Office, Singapore, under its Medium-Sized Centre Programme and the Competitive Research Programme (CRP) (NRF-CRP17-2017-08). This work is also supported by China Scholarship Council (CSC). The authors also thank the Centre for Advanced 2D Materials (CA2DM) for the provided facilities.

Conflict of Interest

The authors declare no conflict of interest.

Data availability statement

The data that support the findings of this study are available from the corresponding author upon reasonable request.

Keywords

AC operation, CMOS compatibility, local excitation, operational lifetime, tunnel junctions

Received: July 30, 2021
Revised: January 26, 2022
Published online: February 20, 2022

[1] J. Lambe, S. L. McCarthy, *Phys. Rev. Lett.* **1976**, *37*, 923.
[2] M. Parzefall, L. Novotny, *ACS Photonics* **2018**, *5*, 4195.
[3] T. J. Duffin, V. Kalathingal, A. Radulescu, C. Li, S. J. Pennycook, C. A. Nijhuis, *Phys. Rev. Appl.* **2020**, *14*, 044021.
[4] H. Qian, S. W. Hsu, K. Gurunatha, C. T. Riley, J. Zhao, D. Lu, A. R. Tao, Z. Liu, *Nat. Photonics* **2018**, *12*, 485.
[5] Q. Q. Shu, W. J. Wen, S. J. Xu, *J. Appl. Phys.* **1989**, *65*, 373.
[6] P. Dawson, D. G. Walmsley, *Surf. Sci.* **1986**, *171*, 135.
[7] L. Yuan, L. Jiang, C. A. Nijhuis, *Adv. Funct. Mater.* **2018**, *28*, 1801710.
[8] T. Morozumi, H. Kaiju, Y. Ohtaka, K. Shiiki, *Jpn. J. Appl. Phys.* **2004**, *43*, 197.
[9] T. Taychatanapat, K. I. Bolotin, F. Kuemmeth, D. C. Ralph, *Nano Lett.* **2007**, *7*, 652.
[10] H. Qian, S. Li, S. W. Hsu, C. F. Chen, F. Tian, A. R. Tao, Z. Liu, *Nat. Commun.* **2021**, *12*, 3111.
[11] C. Zhang, J. P. Hugonin, A. L. Coutrot, C. Sauvan, F. Marquier, J. J. Greffet, *Nat. Commun.* **2019**, *10*, 4949.
[12] M. Parzefall, P. Bharadwaj, A. Jain, T. Taniguchi, K. Watanabe, L. Novotny, *Nat. Nanotechnol.* **2015**, *10*, 1058.
[13] W. Du, T. Wang, H. S. Chu, C. A. Nijhuis, *Nat. Photonics* **2017**, *11*, 623.
[14] P. Bharadwaj, A. Bouhelier, L. Novotny, *Phys. Rev. Lett.* **2011**, *106*, 226802.
[15] F. Wang, Y. Liu, T. J. Duffin, V. Kalathingal, S. Gao, W. Hu, Y. Guo, S. J. Chua, C. A. Nijhuis, *ACS Photonics* **2021**, *8*, 1951.
[16] Y. Lin, T. X. Hoang, H. S. Chu, C. A. Nijhuis, *Nanophotonics* **2021**, *10*, 1145.
[17] S. P. Gurunarayanan, N. Verellen, V. S. Zharinov, F. James Shirley, V. V. Moshchalkov, M. Heyns, J. Van de Vondel, I. P. Radu, P. Van Dorpe, *Nano Lett.* **2017**, *17*, 7433.
[18] J. Kern, R. Kullock, J. Prangsma, M. Emmerling, M. Kamp, B. Hecht, *Nat. Photonics* **2015**, *9*, 582.
[19] R. Kullock, M. Ochs, P. Grimm, M. Emmerling, B. Hecht, *Nat. Commun.* **2020**, *11*, 115.
[20] W. Du, Y. Han, H. Hu, H. S. Chu, H. V. Annadata, T. Wang, N. Tomczak, C. A. Nijhuis, *Nano Lett.* **2019**, *19*, 4634.
[21] J. G. Simmons, *J. Appl. Phys.* **1963**, *34*, 1793.

© 2022 The Authors. Laser & Photonics Reviews published by Wiley-VCH GmbH

18638899, 2022, 5, Downloaded from https://onlinelibrary.wiley.com/doi/10.1002/lpor.202100419 by University Of Twente Finance Department, Wiley Online Library on [18/01/2023]. See the Terms and Conditions (https://onlinelibrary.wiley.com/terms-and-conditions) on Wiley Online Library for rules of use; OA articles are governed by the applicable Creative Commons License

18638899, 2022, 5, Downloaded from https://onlinelibrary.wiley.com/doi/10.1002/lpor.202100419 by University Of Twente Finance Department, Wiley Online Library on [18/01/2023]. See the Terms and Conditions (https://onlinelibrary.wiley.com/terms-and-conditions) on Wiley Online Library for rules of use; OA articles are governed by the applicable Creative Commons License

[22] Y. Gutiérrez, A. S. Brown, F. Moreno, M. Losurdo, *J. Appl. Phys.* **2020**, *128*, 080901.
[23] M. W. Knight, N. S. King, L. Liu, H. O. Everitt, P. Nordlander, N. J. Halas, *ACS Nano* **2014**, *8*, 834.
[24] K. M. McPeak, S. V. Jayanti, S. J. P. Kress, S. Meyer, S. Iotti, A. Rossinelli, D. J. Norris, *ACS Photonics* **2015**, *2*, 326.
[25] G. V. Naik, V. M. Shalaev, A. Boltasseva, *Adv. Mater.* **2013**, *25*, 3264.
[26] D. Y. Fedyanin, D. I. Yakubovsky, R. V. Kirtaev, V. S. Volkov, *Nano Lett.* **2016**, *16*, 362.
[27] V. Mkhitaryan, K. March, E. N. Tseng, X. Li, L. Scarabelli, L. M. Liz Marzán, S. Y. Chen, L. H. G. Tizei, O. Stéphan, J. M. Song, M. Kociak, F. J. García de Abajo, A. Gloter, *Nano Lett.* **2021**, *21*, 2444.
[28] T. G. Habteyes, S. Dhuey, E. Wood, D. Gargas, S. Cabrini, P. J. Schuck, A. P. Alivisatos, S. R. Leone, *ACS Nano* **2012**, *6*, 5702.
[29] D. T. Debu, P. K. Ghosh, D. French, J. B. Herzog, *Opt. Mater. Express* **2017**, *7*, 73.
[30] E. Ricci, R. Novakovic, *Gold Bulletin* **2001**, *34*, 41.
[31] N. Eustathopoulos, *Metals* **2015**, *5*, 350.
[32] K. Iwansson, G. Sinapius, W. Hoornaert, *Measuring Current, Voltage and Power, Handbook of Sensors and Actuators*, Vol. *7* Elsevier Science, **1999**, p. chap. 2.
[33] C. A. Nijhuis, W. F. Reus, G. M. Whitesides, *J. Am. Chem. Soc.* **2009**, *131*, 17814 .
[34] E. O. Filatova, A. S. Konashuk, *J. Phys. Chem. C* **2015**, *119*, 20755.
[35] E. H. Huisman, C. M. Guédon, B. J. van Wees, S. J. van der Molen, *Nano Lett.* **2009**, *9*, 3909.
[36] M. L. Trouwborst, C. A. Martin, R. H. M. Smit, C. M. Guédon, T. A. Baart, S. J. van der Molen, J. M. van Ruitenbeek, *Nano Lett.* **2011**, *11*, 614.
[37] G. Wang, Y. Kim, S.-I. Na, Y. H. Kahng, J. Ku, S. Park, Y. H. Jang, D. Y. Kim, T. Lee, *J. Phys. Chem. C* **2011**, *115*, 17979.
[38] T. Ikuno, H. Okamoto, Y. Sugiyama, H. Nakano, F. Yamada, I. Kamiya, *Appl. Phys. Lett.* **2011**, *99*, 023107.
[39] J. R. Kirtley, T. N. Theis, J. C. Tsang, D. J. DiMaria, *Phys. Rev. B* **1983**, *27*, 4601.
[40] L. Cui, Y. Zhu, M. Abbasi, A. Ahmadivand, B. Gerislioglu, P. Nordlander, D. Natelson, *Nano Lett.* **2020**, *20*, 6067.
[41] K. Z. Rajab, M. Naftaly, E. H. Linfield, J. C. Nino, D. Arenas, D. Tanner, R. Mittra, M. Lanagan, *J. Microelectron. Electron. Packag.* **2008**, *5*, 2.
[42] E. Z. Luo, S. K. Wong, A. B. Pakhomov, J. B. Xu, I. H. Wilson, C. Y. Wong, *J. Appl. Phys.* **2001**, *90*, 5202.
[43] K. Gloos, P. J. Koppinen, J. P. Pekola, *J. Phys. Condens. Matter* **2003**, *15*, 1733.
[44] Q. Q. Shu, W. G. Ma, *Appl. Phys. Lett.* **1992**, *61*, 2542.
[45] K. S. Makarenko, T. X. Hoang, T. J. Duffin, A. Radulescu, V. Kalathingal, H. J. Lezec, H.-S. Chu, C. A. Nijhuis, *Adv. Sci.* **2020**, *7*, 1900291.
[46] C. Féry, B. Racine, D. Vaufrey, H. Doyeux, S. Cinà, *Appl. Phys. Lett.* **2005**, *87*, 213502.
[47] M. Ishii, R&D Rev, *Toyota CRDL* **2003**, *38*, 55.
[48] S. Bhatti, R. Sbiaa, A. Hirohata, H. Ohno, S. Fukami, S. N. Piramanayagam, *Mater. Today* **2017**, *20*, 530.
[49] J. Akerman, P. Brown, M. DeHerrera, M. Durlam, E. Fuchs, D. Gajewski, M. Griswold, J. Janesky, J. J. Nahas, S. Tehrani, *IEEE Trans. Device Mater. Reliab.* **2004**, *4*, 428.
[50] M. Gibbons, S. Kyusik, S. Funada, S. Xizeng, in: IEEE International Magnetics Conference, Amsterdam, Netherlands, August 2002, pp. AV4.
[51] Y. Liu, Y. H. Lee, M. R. Lee, Y. Yang, X. Y. Ling, *ACS Photonics* **2017**, *4*, 2529.
[52] Y. Cui, R. S. Hegde, I. Y. Phang, H. K. Lee, X. Y. Ling, *Nanoscale* **2014**, *6*, 282.
[53] S. D. Rezaei, R. J. Hong Ng, Z. Dong, J. Ho, E. H. H. Koay, S. Ramakrishna, J. K. W. Yang, *ACS Nano* **2019**, *13*, 3580.
[54] M. Mansuripur, A. R. Zakharian, A. Lesuffleur, S.-H. Oh, R. J. Jones, N. C. Lindquist, H. Im, A. Kobyakov, J. V. Moloney, *Opt. Express* **2009**, *17*, 14001.
[55] A. B. Taylor, P. Michaux, A. S. M. Mohsin, J. W. M. Chon, *Opt. Express* **2014**, *22*, 13234.
[56] C. Leon Christopher, A. Rosławska, A. Grewal, O. Gunnarsson, K. Kuhnke, K. Kern, *Sci. Adv.* **2019**, *5*, eaav4986.

© 2022 The Authors. Laser & Photonics Reviews published by Wiley-VCH GmbH